UNIVERSITY OF BRISTOL

Impact damage behavior of lightweight CFRP protection suspender on railway vehicles

Jian Jiang [a], Zhifang Zhang [a],*, Jiyang Fu [a],*, Karthik Ram Ramakrishnan [b], Caizheng Wang [c], Hongxu Wang [d]

[a] Research Center for Wind Engineering and Engineering Vibration, Guangzhou University, Guangzhou 510006, China
[b] Department of Engineering Science, University of Oxford, Oxford OX1 3PJ, UK
[c] School of Aerospace Engineering, Tsinghua University, Beijing 100084, China
[d] School of Engineering and Information Technology, The University of New South Wales, Canberra ACT 2600, Australia

HIGHLIGHTS

- The impact damage behaviour of a lightweight designed CFRP protection suspender on rail vehicles was analysed with considering the bolt preloads.
- The bolt preload can successfully applied on the CFRP protection suspender through reducing the local temperature of the bolt shank.
- The vulnerable positions under impact include the contact region, the curved corner, and the areas around the bolt holes for the CFRP protection suspender.
- The increase of bolt preloads can help to prevent the occurrence of crack damage around the installation holes of the CFRP protection suspender.
- The energy absorption and damage resistance capability of CFRP protection suspender with $[0]_{10}$ layup are much better than $[0/90/0/90/0]_S$.

GRAPHICAL ABSTRACT
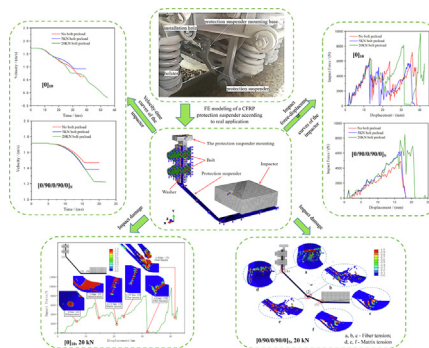
ABSTRACT

The lightweight design of railway vehicle components using fiber reinforced polymers (FRPs) has become a research hotspot due to the strong need for energy saving and environmental protection. This paper aims to evaluate the impact damage behavior of a carbon fiber reinforced polymers (CFRP) protection suspender, which is a component on railway vehicles to prevent the falling joist and bolster from touching the rails and to avoid the derailment of trains. A finite element (FE) model of the CFRP protection suspender, which considered varying bolt preloads was established in ABAQUS/Explicit. The bolt preload was successfully applied around the installation holes on the protection suspender by deliberately reducing the local temperature of the bolt shank to create shrinkage. The impact behavior of the protection suspender was then analyzed, and the impact-induced damage was governed by the Continuum Damage Mechanics (CDM) models, which include both intra-laminar damage and inter-laminar damage. The low-velocity impact response of the CFRP protection suspender was investigated with the lay-ups of $[0]_{10}$ and $[0/90/0/90/0]_S$ under different bolt preloads (i.e. 0, 5 and 20 kN). The results showed that the

---

* Corresponding authors.
    E-mail addresses: 2111816126@e.gzhu.edu.cn (J. Jiang), zfzhang@gzhu.edu.cn (Z. Zhang), jyfu@gzhu.edu.cn (J. Fu), karthik.ramakrishnan@eng.ox.ac.uk (K.R. Ramakrishnan), wang_caizheng@mail.tsinghua.edu.cn (C. Wang), hongxu.wang@adfa.edu.au (H. Wang).

vulnerable positions of the protection suspenders included the contact edge between the protection suspender and the impactor, the curved corner of the suspender, and the areas around the bolt holes. In addition, the protection suspender with the lay-up of $[0]_{10}$ had better impact resistance than that with the lay-up of $[0/90/0/90/0]_S$. By applying different preloads, it showed that the increase of bolt preloads could help to prevent the occurrence of crack damage around the installation holes, thus improving the structural safety when subjected to low-velocity impact. The present simulation results offered great value for the lightweight design and structural optimization of a protection suspender on railway vehicles that had to survive from sudden impact loads in service.

1. Introduction

The demand for energy saving and environmental protection has resulted in the adoption of lightweight design in the rail and automobile industries and the substitution of light and strong materials for the traditional steel components. Fiber reinforced polymers (FRPs), with the advantages of high strength and modulus/weight ratio, superior corrosion resistance and durability, and good designability, have become one of the most suitable and promising candidates to replace the traditional metal components in railway vehicles [1–3]. However, the layer by layer stacking of FRP laminates means that composite structures are susceptible to impact damage. Both experiment and finite element (FE) simulation techniques have been used to study the impact behavior of composite structures. The current practice required to develop and certify new composite structures follows a building block approach starting from basic material characterization using coupon-level testing and moving to more complex structural details [4]. One approach for reducing the development time and cost of composite structures is to increase modeling and simulation at all levels of the product development cycle. Finite element modelling (FEM) can simulate the impact process of a composite structure with lower cost, less time, and satisfactory accuracy in contrast to the large experimental campaign requiring expensive specimen preparation and testing equipment. Moreover, after the model is validated by a small number of experimental cases, the effects of different material properties or impact energies could be easily evaluated using FEM. Therefore, FE simulation has become a common method for studying the impact behavior of composite structures [3,5].

Bogenfeld et al. [6] provided a review of many analytical and numerical models developed for simulating the low-velocity impact behavior of composites. The main objectives of these models are the prediction of delamination, fiber failure and inter-fiber damage. Continuum Damage Mechanics (CDM) models have been widely applied to simulate the damage initiation and propagation of composite materials [7–12]. The CDM models determine whether any damage has occurred by meeting the initial damage criterion (failure criterion), and calculate the damage severity by setting damage status variables and damage evolution rules. The material stiffness in FEM will then be degraded accordingly with the damage status variables. The failure criteria for composite materials are generally developed by considering the failure modes, such as Hashin criterion [13,14], Chang-Chang criterion [15], and Hou criterion [16,17]. In addition, given the laminated structure, the composite is prone to delamination damage. The techniques of simulating delamination damage in FEM include Cohesive Zone Model (CZM) [18,19] and Virtual Crack Closure Technique (VCCT) [20]. The benchmark problems solved by Bogenfeld et al. [6] and many other researchers mainly aim at impact on structures with simple geometries, such as square plates impacted by a hemispherical impactor. However, impact on the real structures, which include holes, bolted joints and other structural features, has been rarely studied.

There are many components and structures on railway vehicles that must withstand impact loads [3,5,21], such as wheels and car bodies, bolster protection suspenders, etc. Gao et al. [21] provided a review of composites in crashworthiness applications for rail vehicles. If these components or structures are designed using FRP composite materials for lightweight, special attention should be paid to the analysis of such structures under impact loads. Currently, there are scarcely any studies on the lightweight design of protection suspenders used in bogies. Only a few reports have studied the base components of the bogies on which the protection suspender are mounted. A typical protection suspender and its installation on the bogie are shown in Fig. 1(a) and (b) [22]. In normal circumstances, the bolster is supported on the bogie and has no impact on the protection suspender. However, once the bolster falls off due to accidental reasons, the protection suspender will have to bear the impact load of the falling bolster to prevent it from touching the rails, thereby avoiding the derailment of trains.

Feng [23] investigated the cracked mounting base of protection suspenders and concluded that the cause of the fracture on the mounting base had involved various aspects such as smelting, design, manufacturing, assembly, maintenance and operation management. Lian et al. [22] studied the fatigue failure mechanism of the mounting base of the protection suspender by FEM and experiment. They found that the resonance between the protection suspender and the mounting base caused fatigue cracks on the mounting base and around the installation holes of the protection suspender. They proposed multiple improvements, such as manufacturing the bases with stronger materials, adding gaskets on both sides of the bolt holes on the protection suspender, and changing the structure of the protection suspender to reduce the resonance. Replacing the steel protection suspender to one made of lightweight FRP laminates will also modify the modal parameters and avoid the problems related to resonance between the composite suspender and the steel mounting base.

In this paper, a three-dimensional FE model was developed in ABAQUS/Explicit to study the impact behavior of a CFRP protection suspender. In the impact analysis of the protection suspender, the damage model of the FRP composites was based on the CDM which was implemented as a user-material (VUMAT) subroutine to calculate the damage status of the elements and then update the elements' stress and energy. The CZM and cohesive elements were used to analyze and evaluate the delamination damage that might occur after the impact on the protection suspender. The cohesive zone method can overcome the problems associated with the VCCT method, which requires a predefined initial crack location [12,24]. So CZM has been widely used and reported in the literature to simulate the delamination damage in composite materials [4,25,26]. Bolt connections are usually used between the protection suspender and its mounting base, and it is necessary to consider the effect of bolt preloads on the installation holes in the analysis of the impact response of the protection suspender. Since the bolt tool is not available in the current ABAQUS/Explicit module, a virtual thermal deformation method was adopted to apply preloads
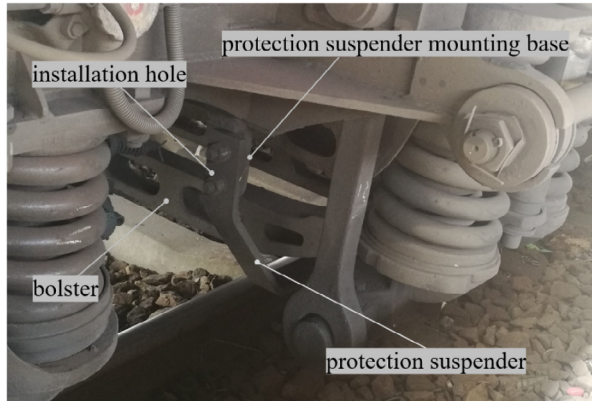
(a) Real view of the bogie with protection suspender

full view of protection suspender
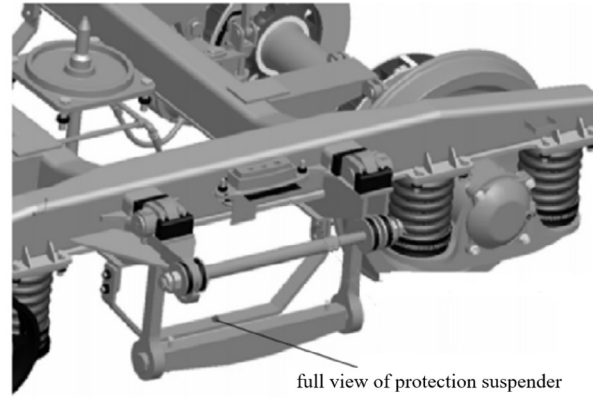
(b) Diagram of the bogie with protection suspender [22]

Fig. 1. Protection suspender and its installation on the bogie of a rail vehicle.

[27–31]. The coefficient of orthotropic thermal expansion was defined for the bolt material, and the reduction of temperature caused the bolt to shrink along the shank, resulting in bolt preload [27].

2. The constitutive model of FRP composite

During the impact process, the mechanical properties of the FRP materials deteriorate after the damage initiates. When the strain increases to meet the failure criteria, the material is failed completely. In this paper, the CDM model was used to determine whether damage occurred in the material by the initial criterion. The damage severity was calculated by introducing the variables of damage status and the damage evolution law. In addition, the intra-laminar damage (i.e. the damage within each layer) and inter-laminar damage (i.e. the delamination between adjacent plies) were both considered in the impact model of protection suspender.

2.1. Intra-laminar damage

2.1.1. Failure initial criteria

The Hashin criterion [14] has been widely adopted in the numerical analysis of composite materials because it has good accuracy in impact simulations and has separated the failure modes, thus it is easy to be used for analyzing the cause of damage. In this paper, the three-dimensional expression of the Hashin criterion was used as the initial damage criterion. Huang and Lee [32] have shown through experiments that the stress of the composite material changes dramatically and may be discontinuous during the impact process, while the strain changes continuously. So the Hashin criterion in the form of strain is more applicable to describe the failure of composite materials. The three-dimensional Hashin criterion expressed in the form of strain is as follows [32–35]:

Fiber tensile failure: $\varepsilon_{11} > 0$

$$e_{ft} = \left(\frac{\varepsilon_{11}}{X_T^\varepsilon}\right)^2 + \alpha\left(\frac{\varepsilon_{12}}{S_{12}^\varepsilon}\right)^2 + \alpha\left(\frac{\varepsilon_{13}}{S_{13}^\varepsilon}\right)^2 \tag{1}$$

Fiber compressive failure: $\varepsilon_{11} < 0$

$$e_{fc} = \left(\frac{\varepsilon_{11}}{X_C^\varepsilon}\right)^2 \tag{2}$$

Matrix tensile failure : $\varepsilon_{22} + \varepsilon_{33} > 0$

$$e_{mt} = \left(\frac{\varepsilon_{22} + \varepsilon_{33}}{Y_T^\varepsilon}\right)^2 + \frac{1}{S_{23}^{\varepsilon\,2}}\left(\varepsilon_{23}^2 - \frac{E_{22}E_{33}}{G_{23}^2}\varepsilon_{22}\varepsilon_{33}\right) + \left(\frac{\varepsilon_{12}}{S_{12}^\varepsilon}\right)^2 + \left(\frac{\varepsilon_{13}}{S_{13}^\varepsilon}\right)^2 \tag{3}$$

Matrix compressive failure : $\varepsilon_{22} + \varepsilon_{33} < 0$

$$e_{mc} = \left(\frac{E_{22}\varepsilon_{22} + E_{33}\varepsilon_{33}}{2G_{12}S_{12}^\varepsilon}\right)^2 + \left(\frac{\varepsilon_{22} + \varepsilon_{33}}{Y_C^\varepsilon}\right)\left[\left(\frac{E_{22}Y_C^\varepsilon}{2G_{12}S_{12}^\varepsilon}\right)^2 - 1\right] + \left(\frac{\varepsilon_{12}}{S_{12}^\varepsilon}\right)^2 + \left(\frac{\varepsilon_{13}}{S_{13}^\varepsilon}\right)^2$$
$$+ \left(\frac{1}{S_{23}^\varepsilon}\right)^2\left(\varepsilon_{23}^2 - \frac{E_{22}E_{33}}{G_{23}^2}\varepsilon_{22}\varepsilon_{33}\right) \tag{4}$$

where $\varepsilon_{ij}(i, j = 1, 2, 3)$ is the strain tensor, and the subscripts of "T" and "C" indicate "tension" and "compression", respectively. Thus, $X_T^\varepsilon, X_C^\varepsilon, Y_T^\varepsilon, Y_C^\varepsilon$ are the initial strain strength under the tension and compression in the "X" direction (along the fiber) and in the "Y" direction (perpendicular to the fiber direction), respectively. $S_{12}^\varepsilon, S_{13}^\varepsilon, S_{23}^\varepsilon$ are the initial shear strain strength. The above initial strain strength is determined by the following relationship:
$X_T^\varepsilon = X_T/E_{11}, X_C^\varepsilon = X_C/E_{11}, Y_T^\varepsilon = Y_T/E_{22}, Y_C^\varepsilon = Y_C/E_{22}$

$S_{12}^\varepsilon = S_{12}/G_{12}S_{13}^\varepsilon = S_{13}/G_{13}S_{23}^\varepsilon = S_{23}/G_{23}$

where X_T, X_C, Y_T, Y_C are the initial stress strength under the tension and compression in the "X" and "Y" direction, while S_{12}, S_{13}, S_{23} are the initial shear stress strength. The coefficient α in Eqn. (1) represents the contribution of shear stress in the failure of fiber tension, and it was taken as 1 in this paper. In Eqns. (1)-(4), $e_I(I = ft, fc, mt, mc)$ is the failure factor for the corresponding mode. When $e_I \geqslant 1$, the damage of the corresponding mode occurs, and the stiffness of the materials will be reduced accordingly.

2.1.2. Damage evolution law

When the failure factor $e_I(I = ft, fc, mt, mc) \geqslant 1$, damage initiates in materials. With the release of strain energy, the materials enter the softening stage, i.e. the evolution of damage. With the accumulation of damage, strain localization in the FE model will make the energy dissipated in the elements depending on the mesh density, which will reduce the model accuracy. Lapczyk et al. [36] and Linde et al. [37] have reduced the effect of the strain localization by introducing the characteristic length of elements. In this paper, the relationship between energy release rate and the element's characteristic length was set as [12,36]:

$$G_C = \frac{1}{2}\sigma_{eq}^0\varepsilon_{eq}^f L_c \tag{5}$$

where L_C is the characteristic length of the element and it is calculated by Eqn. (6) according to A_{IP} (the area associated with an integration point) and θ (the angle between the mesh line and the crack direction), $G_C, \sigma_{eq}^0, \varepsilon_{eq}^f$ are the energy release rate, the initial equivalent stress and the equivalent strain at the moment of failure, respectively.

$$L_C = \frac{\sqrt{A_{IP}}}{\cos\theta}; \quad |\theta| \leqslant 45° \tag{6}$$

In the CDM model, the degradation of material properties depends on the damage severity of the materials. The damage extent of materials is considered by introducing the damage status variables, which is defined as [12,36]:

$$d_I = \frac{\delta_{I,eq}^f \left(\delta_{I,eq} - \delta_{I,eq}^0 \right)}{\delta_{I,eq} \left(\delta_{I,eq}^f - \delta_{I,eq}^0 \right)}; \quad (I = ft, fc, mt, mc) \tag{7}$$

where d_I is the damage status variables corresponding to the damage modes, $\delta_{I,eq}^0$, $\delta_{I,eq}$, $\delta_{I,eq}^f$ are the equivalent displacement at the beginning of damage, real-time equivalent displacement and equivalent displacement when materials reach complete failure. $\delta_{I,eq}^0$ and $\delta_{I,eq}^f$ are set as follows:

$$\delta_{I,eq}^0 = \frac{\delta_{I,eq}}{\sqrt{e_I}} \tag{8}$$

$$\delta_{I,eq}^f = \frac{2G_{IC}}{\sigma_{I,eq}^0} \tag{9}$$

$$\sigma_{I,eq}^0 = \frac{\sigma_{I,eq}}{\sqrt{e_I}} \tag{10}$$

where G_{IC} is the energy release rate for the corresponding damage mode, and $\sigma_{I,eq}^0$, $\sigma_{I,eq}$ are the initial equivalent stress strength and real-time equivalent stress for the corresponding mode.

The damage state variables of elements calculated by equivalent displacement are required to define the real-time equivalent displacement $\delta_{I,eq}$ in Eqns. (7) and (8) and the real-time equivalent stress $\sigma_{I,eq}$ in Eq. (10). The calculation schemes of the real-time equivalent displacement and real-time equivalent stress for each damage mode are shown in Table 1.

2.2. Inter-laminar damage

Delamination is a common type of damage during the impact process of FRP laminates. For the delaminated damage of the FRP protection suspender, the CZM [18,19] based on the continuous damage mechanics was used in this paper. For the delamination damage between FRP plies, because the damage mostly propagates under the mixed loadings, the quadratic stress failure criterion was adopted as the initiation criterion and the delamination propagation was predicted by the B-K criterion [38]. The expressions for the quadratic stress and B-K criterion are shown in Eqns. (11) and (12).

$$\frac{\langle t_n \rangle^2}{N^2} + \frac{t_s^2}{S^2} + \frac{t_t^2}{T^2} = 1 \tag{11}$$

where t_n is the normal traction stress, t_s and t_t are the shear traction stress, and N, S and T are the corresponding inter-laminar normal and shear stress strength.

$$G^C = G_n^C + \left(G_s^C - G_n^C \right) \left(\frac{G_S}{G_T} \right)^\eta \tag{12}$$

where $G_S = G_s + G_t$, $G_T = G_n + G_S$, G_n, G_s and G_t are the energy release rate for the modes of type I, type II, and type III, respectively, and η is a B-K criterion parameter, of which the value is generally set as 1 to 2 according to the experimental results.

2.3. The verification of VUMAT subroutine

In this paper, the damage model used for the FRP protection suspender was written as a VUMAT subroutine using Fortran and was then incorporated in ABAQUS/Explicit. To verify the validity of the VUMAT subroutine, the results predicted by the present damage model was compared with the impact testing results given by Shi et al. [9].

In their experimental work, composite laminates, with a stacking sequence of [0/90]$_{2S}$, a total thickness of 2 mm and in-plane size of 100 mm × 100 mm, were clamped between two steel plates with a circular exposed area of 75 mm in diameter. A 15-mm diameter cylindrical impactor with a hemispherical head fell from a height of 0.75 m to impact the central area of the tested laminates. The mass of the used impactor was 1, 1.5 and 2 kg resulting in impact energies of 7.35, 11.03 and 14.7 J, respectively.

The numerical simulation based on the experiment performed by Shi et al. [9] was carried out to predict the damage of composite laminates under low-velocity impact. In the present simulation, the composite laminate is established as a panel with a 75 mm diameter and a fully fixed edge. Regarding the mesh of the laminate model, the eight-node solid element (C3D8R) with 0.25 mm thickness is used for each ply, and the eight-node cohesive element (COH3D8) with zero thickness was applied for each interface to simulate the delamination. The material properties used for unidirectional lamina and cohesive elements are listed in Tables 2 and 3, and the comparison of results can be seen in Figs. 2 and 3.

Fig. 2(a, b, c) shows the impact force–time curves under three different impact energies of 7.35, 11.03 and 14.7 J. The simulated impact force–time curves shows good agreement with the experimental curves. The peak impact force and the corresponding occurrence time in experiments are (3116 N, 1.61 ms), (3765 N, 1.97 ms), and (4605 N, 2.13 ms) for impact energy of 7.35, 11.03, and 14.7 J, respectively. In the current simulation, the predicted values are (3338 N, 1.52 ms), (3691 N, 1.98 ms), and (4137 N, 2.12 ms), respectively, which are close to the experimental results. Fig. 2(d, e, f) shows the impact force–displacement curves under the three impact energies. From these figures, we can see that the impact force–displacement curves predicted by the present damage model are near to the experiment data. Especially for the rising slope and the maximum displacement, there is a narrow difference between the prediction and experiment. Fig. 2(g, h, i) shows the absorbed energy-time curves under the impact energy of 7.35, 11.03 and 14.7 J. As can be seen, from the moment of initial contact between the impactor and the laminate till the kinetic energy of impactor is completely absorbed, the simulation curves are generally in good agreement with the experiment. At the

Table 1
Real-time equivalent displacement and real-time equivalent stress for each damage mode.

Damage Modes	Real-time equivalent displacement $\delta_{I,eq}$	Real-time equivalent stress $\sigma_{I,eq}$
Fiber tension	$L_C \sqrt{\varepsilon_{11}^2 + \alpha \varepsilon_{12}^2 + \alpha \varepsilon_{13}^2}$	$\frac{L_C (\sigma_{11}\varepsilon_{11} + \alpha \sigma_{12}\varepsilon_{12} + \alpha \sigma_{13}\varepsilon_{13})}{\delta_{ft,eq}}$
Fiber compression	$L_C \sqrt{\varepsilon_{11}^2}$	$\frac{L_C \sigma_{11}\varepsilon_{11}}{\delta_{fc,eq}}$
Matrix tension	$L_C \sqrt{\varepsilon_{22}^2 + \varepsilon_{33}^2 + \varepsilon_{12}^2 + \varepsilon_{23}^2 + \varepsilon_{13}^2}$	$\frac{L_C (\sigma_{22}\varepsilon_{22} + \sigma_{33}\varepsilon_{33} + \sigma_{12}\varepsilon_{12} + \sigma_{23}\varepsilon_{23} + \sigma_{13}\varepsilon_{13})}{\delta_{mt,eq}}$
Matrix compression	$L_C \sqrt{\varepsilon_{22}^2 + \varepsilon_{33}^2 + \varepsilon_{12}^2 + \varepsilon_{23}^2 + \varepsilon_{13}^2}$	$\frac{L_C (\sigma_{22}\varepsilon_{22} + \sigma_{33}\varepsilon_{33} + \sigma_{12}\varepsilon_{12} + \sigma_{23}\varepsilon_{23} + \sigma_{13}\varepsilon_{13})}{\delta_{mt,eq}}$

Table 2
Material properties of unidirectional lamina [9].

$\rho/(kg/m^3)$	E_{11}/GPa	$E_{22}, E_{33}/GPa$	v_{12}/v_{13}	v_{23}	$G_{12}, G_{13}/GPa$	G_{23}/GPa	X_T/MPa	X_C/MPa
1600	153	10.3	0.3	0.4	6	3.7	2537	1580
Y_T/MPa	Y_C/MPa	$S_{12}, S_{13}/MPa$	S_{23}/MPa	$G_{ft}/(N/mm)$	$G_{fc}/(N/mm)$	$G_{mt}/(N/mm)$	$G_{mc}/(N/mm)$	
82	236	90	40	91.6	79.9	0.22	1.1	

Table 3
Material properties of cohesive elements [9].

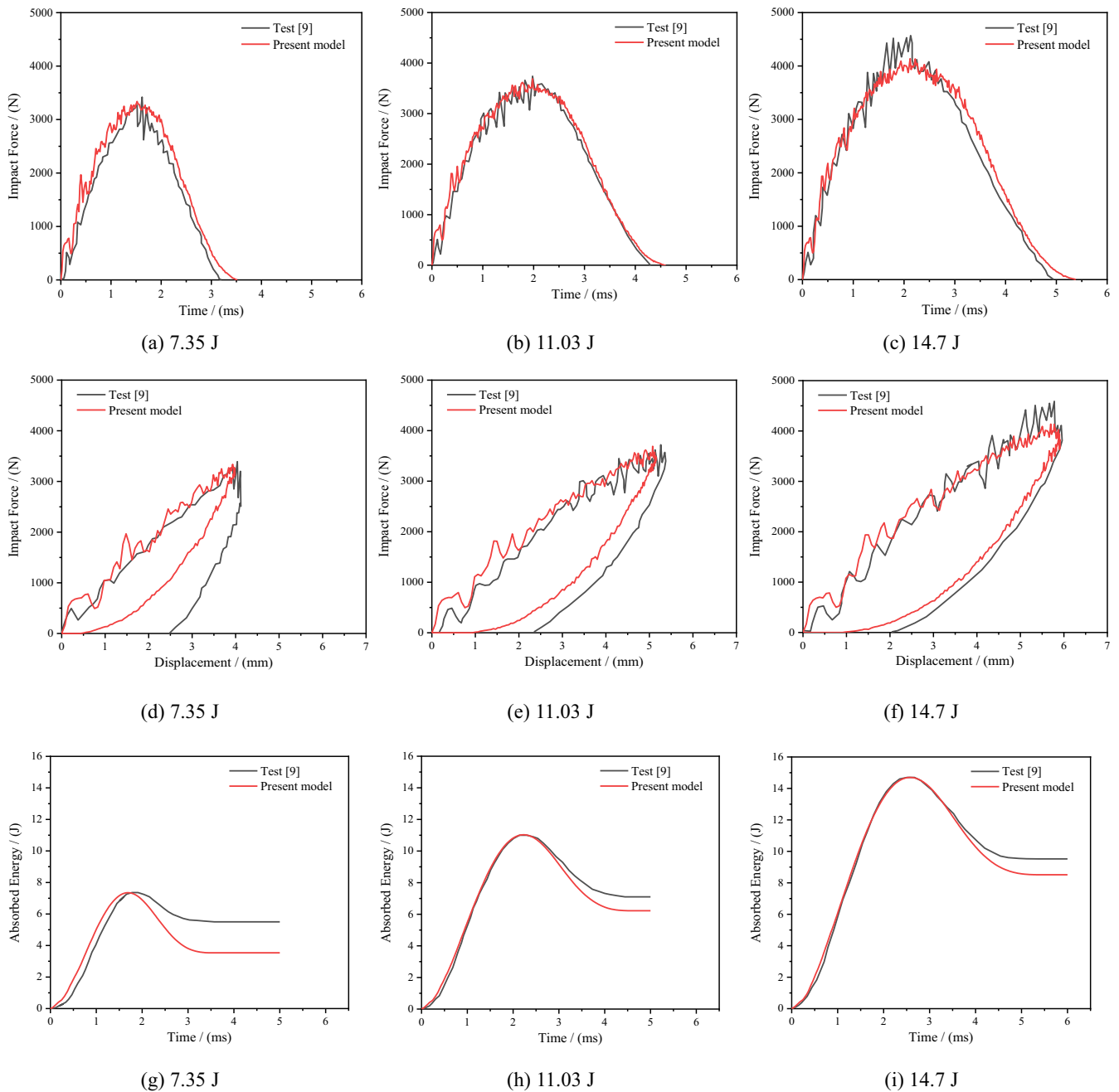| $K_n, K_s, K_t/(GPa/mm)$	N/MPa	$S, T/MPa$	$G_n/(N/mm)$	$G_s, G_t/(N/mm)$	η
6	62.3	92.3	0.28	0.79	1.45

Fig. 2. Comparison of impact force–time curves(a, b, c), impact force–displacement curves(d, e, f) and absorbed energy-time curves(g, h, i) under the impact energy of 7.35, 11.03 and 14.7 J.
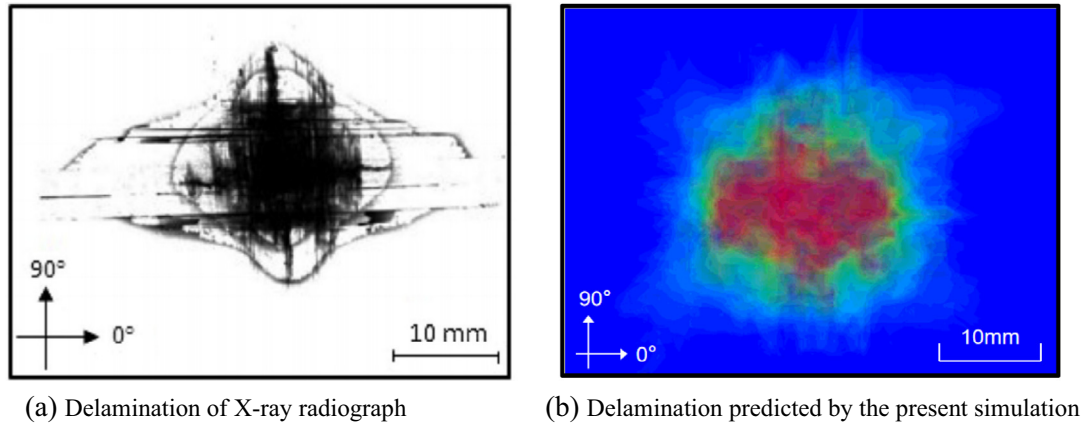
(a) Delamination of X-ray radiograph

(b) Delamination predicted by the present simulation

Fig. 3. Comparison of delamination damage under the impact energy of 14.7 J.

rebound stage of the impactor, the absorbed energy decreases due to the release of elastic strain energy of composite laminates. In the final period of the impact, the impactor loses contact with the laminate, so the absorbed energy remains at a constant value, wherein the simulated curve is always a little lower than the experiment. When the impact energy is relatively low, the response in CFRP panels caused by the impactor is small and the sensors might be less sensitive to capture the signals during impact, so the gap between the simulation and the testing results for 7.35 J has seen a larger discrepancy than those for 11.03 and 14.7 J.

Fig. 3 (a) shows the real delamination damage in the laminate after impact by X-ray scanning and Fig. 3 (b) shows all the superposed delaminations of the laminate predicted by the present damage model. By comparing Fig. 3(a) and (b), it can be seen that the simulated morphology and size of delamination in the laminates are in good agreement with the experimental result.

According to the comparison between the simulation results based on the VUMAT subroutine and the experimental results, the composite damage model established in this paper can effectively simulate the damage caused by impact, and it can confidently be further applied to the impact model of the FRP protection suspender.

3. Finite element modeling of CFRP protection suspender

3.1. Geometric model

The dimensions of the CFRP protection suspender model established in this paper are shown in Fig. 4. There are total 10 sub-laminates with the nominal thickness of 8 mm, and each sub-laminate has 4 layers of the same ply angle. In order to simulate the delamination damage in the protection suspender after impact, the cohesive elements with finite thickness were inserted between FRP sub-laminates. There are 9 cohesive layers in total, and each layer has a thickness of 0.04 mm. To keep consistent with the boundary conditions in real application, the bolt and mounting base with installation holes were included in this modeling. The bolt is with the shape of hexagon, and its geometrics and dimensions are shown in Fig. 5(a). The dimensions and geometric model of the mounting part of the protection suspender base is shown in Fig. 5(b). To make the preloads and stress distributed on the protection suspender evenly, the metal washer was adopted in the model and its geometric model and dimensions are shown in Fig. 5(c). In the engineering application, the mounting bases are fixed on the bogie, and the protection suspender and washer are connected with the mounting base through bolts. The shape of

the steel impact object is a cuboid and its dimensions is 400 mm × 400 mm × 70 mm.

3.2. Material properties and contact settings

In this paper, the material properties of CFRP in literature [9] were used for the protection suspender, and they are listed in Tables 2 and 3, respectively. The protection suspender mounting base, washer and bolt were all given the typical metal properties, its elastic modulus is 210 GPa, Poisson's ratio is 0.3, and density is 7800 kg/m^3. The mass of spring joist about 260 kg according to Wu' study [39] and the mass of bolster is 400 kg approximately in line with the research of Huang et al. [40]. In this paper, the total mass of the spring joist and bolster was thus considered to be 800 kg (to allow some tolerance). Since there are two protection suspenders installed on both sides of the bogie, it is assumed that the mass of the impactor falling on a single protection suspender is 400 kg.

The discrete coordinate was set to determine the material direction of the protection suspender (Fig. 6). The direction along the curved surface of protection suspender is the fiber direction, P-1 as seen in Fig. 6. The normal direction of the protection suspender's surface, N-3 in Fig. 6, is the out of plane direction of the laminates.

Contact interactions were defined for the interface between the protection suspender, impactor, bolt, protection suspender mounting base and the washer. The penalty function with the friction coefficient of 0.3 was set to calculate the contact force between the contact surfaces. During the impact process, the stiffness of the elements in the protection suspender were reduced if the material failure occurs completely. After the elements being degraded, a new contact relationship will generate between the elements adjacent to those with material failure. In addition, during the impactor penetrated the FRP protection suspender, there might be new contact surfaces created between impactor, bolt, mounting base and washer. Therefore, an internal contact was established between the internal elements of the protection suspender, as well as between the internal elements and the impactor, bolt, mounting seat and washer.

3.3. Element type and mesh density

The modeling of FRP protection suspender was established by using the eight-node solid element with reduced integration (C3D8R). Considering the influence of hourglass, the relax stiffness method is used to avoid the fake deformation. As regard to the inter-laminar model, the cohesive element (COH3D8) with finite thickness (0.04 mm) was inserted between plies for simulating
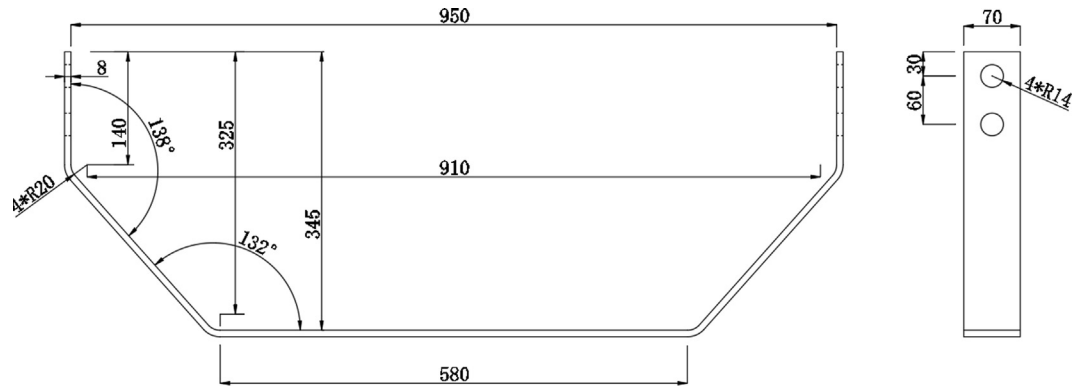
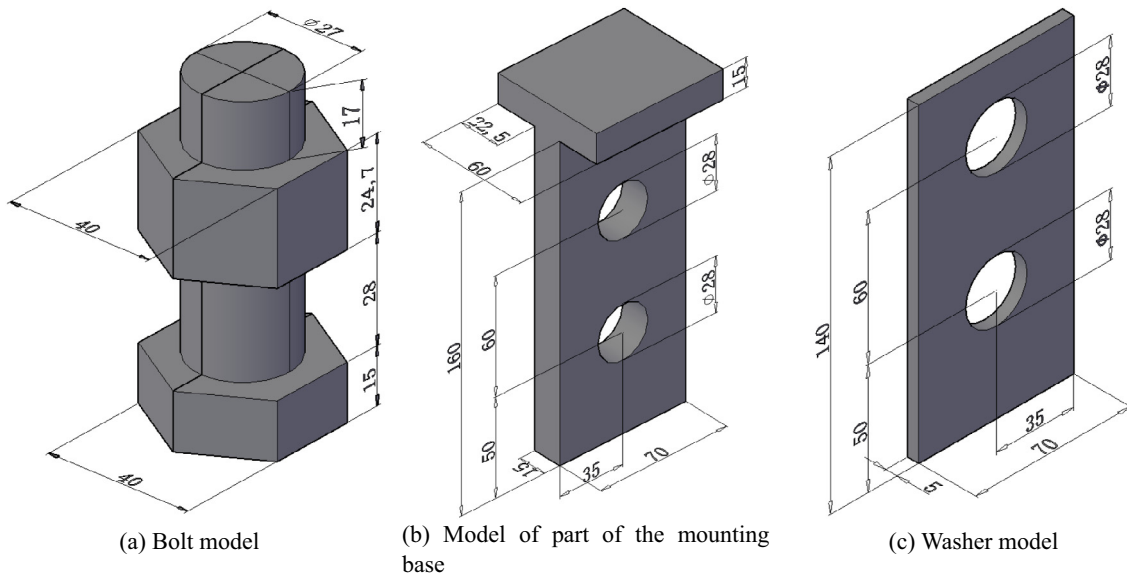**Fig. 4.** The dimensions of the protection suspender (Unit: mm).

(a) Bolt model

(b) Model of part of the mounting base

(c) Washer model

Fig. 5. Geometric model and dimensions of the components (Unit: mm).

P-1 indicates the orientation along the fiber
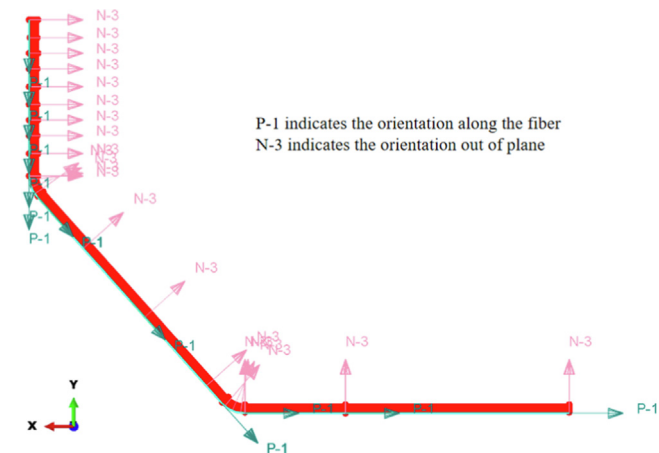N-3 indicates the orientation out of plane

Fig. 6. Fiber orientation and the out-of-plane direction of the composite protection suspender.

the delamination initiation and propagation. Meanwhile, C3D8R element was also used for bolt, protection suspender mounting base and washer. The impactor was modeled as a rigid body, and the corresponding element type was R3D4.

For the meshing of FRP protection suspender, the element size was 1 mm in the width direction of the protection suspender, 1 mm × 1 mm in the two curved areas of the protection suspender and the contact edges where the impactor touches protection suspender. After meshing, the element number of protection suspender was 314792, of which C3D8R element number was 165680, and the number of cohesive element (COH3D8) was 149112. The global size control was adopted for bolt, and the global size was set as 3.2 mm. The total element number of two bolts was 3306.

3.4. Impact model of protection suspender

As for the lay-ups design of the CFRP protection suspender, both $[0]_{10}$ and $[0/90/0/90/0]_S$ are considered. On the one hand, protection suspender is beam-like structure which is an elongated component and shows the bending behavior like a beam when subjected to low velocity impact. The $[0]_{10}$ layup will have all the carbon fiber placed along the beam length and may provide more effective load bearing. On the other hand, for a composite structure in which fibers are arranged in one direction (all 0°), it may be prone to the damage caused by transverse matrix tension and this is especially concerned for the protection suspender where bolt holes exist. With some 90°layers, the transverse tension resistance

may be improved. Besides, in industry the protection suspender can be manufactured using woven fabric FRP prepregs. Therefore, the lay-up of [0/90/0/90/0]$_S$ was also considered for designing the composite protection suspender in this paper.

The impact model of FRP protection suspender was established in ABAQUS, as shown in Fig. 7. Considering the symmetry of the model, 1/4 of the original model was simulated so that to save the calculation time. The impactor (the mass is 100 kg in 1/4 model) was desired to fall from the height of 0.15 m (according to the real joint falling case), but to improve the calculation efficiency, the impactor was set just about contacting the protection suspender (very close distance) and the initial velocity on the impactor was set to be 1.7146 m/s, calculated by the falling height and the corresponding initial kinetic energy. In this modeling, the protection suspender mounting base and the steel washers were set as rigid bodies. The displacement in all directions of the reference point of the protection suspender mounting base was constrained to zero. For the washer, only the translation displacement in the direction along the length of the bolt shank was released, while the displacement in other directions were constrained to zero. In addition, symmetry constraints were also imposed on each symmetrical plane.

3.5. Preloading of bolt

By defining the thermal expansion coefficient, the bolt shank will shrink under the negative temperature loads, which will drive the nut to compress the metal washers to form the preloads. The bolt material properties are shown in Table 4. As can be seen, an orthotropic thermal expansion coefficient was given to the bolts since only the axial direction of the bolt shank needs to shrink to form the compression force on the metal washers. Meanwhile, the coordinate defined for the bolt material follows a principle that the direction of the non-zero thermal expansion coefficient (α_{33} in Table 4) is along the length of the bolt shank.

To include the bolt preloads in the impact model, the preloads need to be applied before the impactor contacts the protection suspender. Two analysis steps were conducted. In the first step, the bolt preloads were applied by using the cooling method. A preliminary study has been conducted to understand the relationship between temperature loads and bolt preload. The typical CFRP material properties from literature [9] have been defined in the model and it has shown a linear relationship between the bolt force and the temperature loads (Fig. 8). To apply an expected bolt

preload, linear interpolation can be used to determine the equivalent temperature loads to be applied on the bolts. The bolt preloads in the protection suspender model were designed to be 0, 5 and 20 kN, and the corresponding equivalent temperature loads were applied as 0 ℃, −15 ℃, −60 ℃. The temperature loads were kept consistent till the end of the second analysis step so that the preloads can be maintained through the both analysis steps. The step two is the impact analysis.

4. Results and discussions

To study the influence of different layups and bolt preloads on the impact resistance of CFRP protection suspender, the low-velocity impact behavior with considering different bolt preloads for the two CFRP protection suspenders ([0]$_{10}$ and [0/90/0/90/0]$_S$) was carried out.

4.1. Impact velocity and energy absorption

The velocity–time curves of impactor are shown in Fig. 9 for two kinds of CFRP protection suspenders being impacted under different bolt preloads. It can be seen that, after the second analysis step (t = 5 ms) begins, the impactor hit the protection suspender and its speed gradually decreased. When 0 and 5 kN preloads were applied, the velocity of impactor on the impact model of the [0]$_{10}$ and [0/90/0/90/0]$_S$ protection suspender remained unchanged after it dropped to a certain extent, indicating that the impactor completely penetrated the protection suspender. When the bolt preload was 20 kN, the velocity of impactor remained unchanged after it dropped to a certain extent in the case of [0/90/0/90/0]$_S$ protection suspender, indicating the penetration occurs. However, for the [0]$_{10}$ protection suspender, velocity of impactor continued to drop till 0 m/s, and then the velocity has turned the direction and increased, indicating that [0]$_{10}$ protection suspender was not broken or not broken completely so that the impactor was rebounded after the kinetic energy of impactor was fully absorbed. During the impact, when the bolt preload were 0, 5 and 20 kN, the minimum velocity of impactor for the [0]$_{10}$ protection suspender were 0.6101 m/s, 0.9257 m/s and 0, the corresponding energy absorbed by protection suspender were 128.39 J, 104.15 J and 147.00 J. While for the [0/90/0/90/0]$_S$ protection suspender, the minimum velocity of impactor were 1.4660 m/s, 1.3821 m/s and 1.2212 m/s, the corresponding energy absorbed by protection suspender were 39.54 J, 51.49 J and 72.43 J. It reveals that the energy absorption capacity of the [0]$_{10}$ protection suspender is remarkably higher than that of the [0/90/0/90/0]$_S$ protection suspender. Moreover, when the bolt preload was 0 and 5 kN, the [0]$_{10}$ protection suspender was penetrated, but when the bolt preload was 20 kN, the [0]$_{10}$ protection suspender was not penetrated or not completely penetrated. For the [0/90/0/90/0]$_S$ protection suspender, as the bolt preload increased from 0, 5 to 20 kN, the speed of impactor takes longer to reach the minimum and the energy absorption of protection suspender had a stable growth. Therefore, it can be inferred that by increasing the bolt preload, the energy absorption capacity of the protection suspender can be improved and the propagation of damage will slow down, thus will improve the safety of the protection suspender during low-velocity impact.

4.2. Impact force

The impact force–displacement curves of the impactor are shown in Fig. 10(a) for the [0]$_{10}$ protection suspender being constrained under three different bolt preloads. During the initial contact between the impactor and the protection suspender (impactor
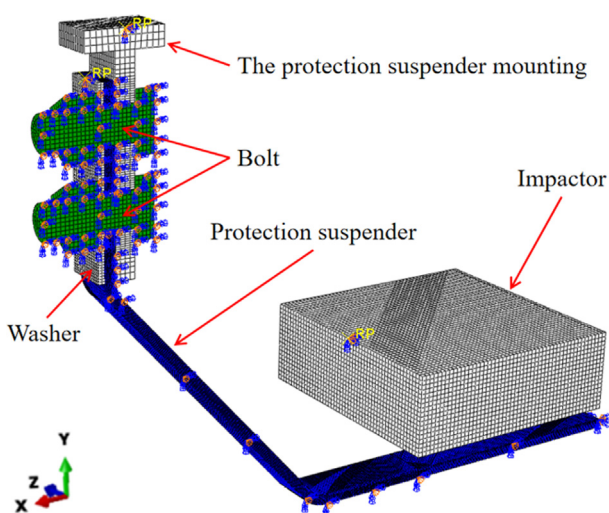

Fig. 7. Impact model of composite protection suspender (1/4 model).

Table 4
Material properties of steel bolt.

ρ/kg/m^3	E/GPa	v	α_{11}, α_{22}/℃$^{-1}$	α_{33}/℃$^{-1}$
7800	210	0.3	0	1.2e-5

Note: α_{11}, α_{22}, α_{33} are the thermal expansion coefficients corresponding to the three directions of material coordinate. The referenced initial temperature is 0 ℃.
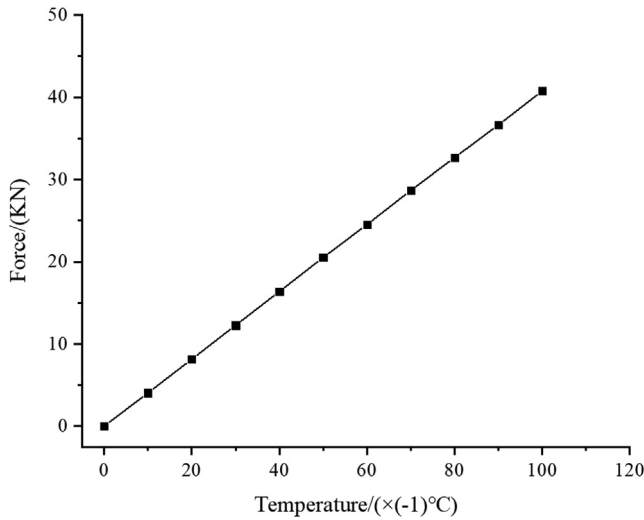

Fig. 8. Bolt force-temperature loads curves for a typical composite materials.

displacement increasing from 0 mm to approximate 13 mm), the impact force increased monotonically and reached a peak. Then, the impact force dropped dramatically and oscillated severely as the impactor continued to deform the protection suspender. More peaks of the impact force in the curves can be seen during the impact. This curve trend could be explained as follows. In the initial ascending curve, the protection suspender started from undamaged and elastic status to with accumulated local microdamage. The first inflection point indicates the occurrence of macro damage (big delamination area, fiber breakage, etc.) in the protection suspender, so the impact force began to drop rapidly till

the macro damage propagated to the end and the impact force began to go up again. There are multiple subsequent peaks in the curve, each of which indicated a macro damage has occurred in the plies of the protection suspender. As can be seen in Fig. 10 (a), for the models having applied preloads of 0 kN and 5 kN, the impact force finally reduced to 0, which means the impactor has penetrated the FRP suspender. For the model with 20 kN preloads, the displacement of impactor eventually decreased, which can be inferred that the impactor was rebounded and the protection suspender was not penetrated. For the [0/90/0/90/0]$_S$ protection suspender, as seen in Fig. 10(b), there appeared only one peak, then the impact force dropped rapidly to 0, which indicated that the protection suspender had suffered severe damage and completely destroyed. For the model with 0, 5 or 20 kN bolt preloads, there are no significant difference in the performance of impact resistance, in terms of being destroyed or not. But with 20 kN preloads, the collapse of the FRP structure is prolonged and the energy absorption is higher. By comparing Fig. 10(a) and (b), [0]$_{10}$ protection suspender is much better in the impact resistance than that of [0/90/0/90/0]$_S$.

4.3. Impact damage

Fig. 11 shows the impact force–displacement curve of impactor ([0]$_{10}$ FRP protection suspender with 20 kN bolt preload) along with the pictures showing damage status of protection suspender at different running time. In the figure, (1), (2) and (3) represents the location in the protection suspender to be focused on for observing the damage. In the initial stage that the displacement of impactor increased from 0 mm to about 13 mm, some signs of delamination damage can be seen ("t = 5 ms" is shown) at the position (1). At t = 9 ms, severe delamination occurred at position (2) and a significant force decrease appeared for the first time. Then at t = 13.5 ms, the convex surface and some serious matrix tension damage appeared at the position (3), after another sharp decline the impact force. The damage continued to develop, and a certain degree of fiber tensile damage occurred at t = 15.5 ms. As the impact force continued, the stress at position (3) kept being concentrated due to the punch from the edge of impactor, and the obvious hollow was observed at t = 24 ms. At the same time, the tensile damage of fiber propagated and it was accompanied by apparent delamination, so the impact force has dropped drasti-
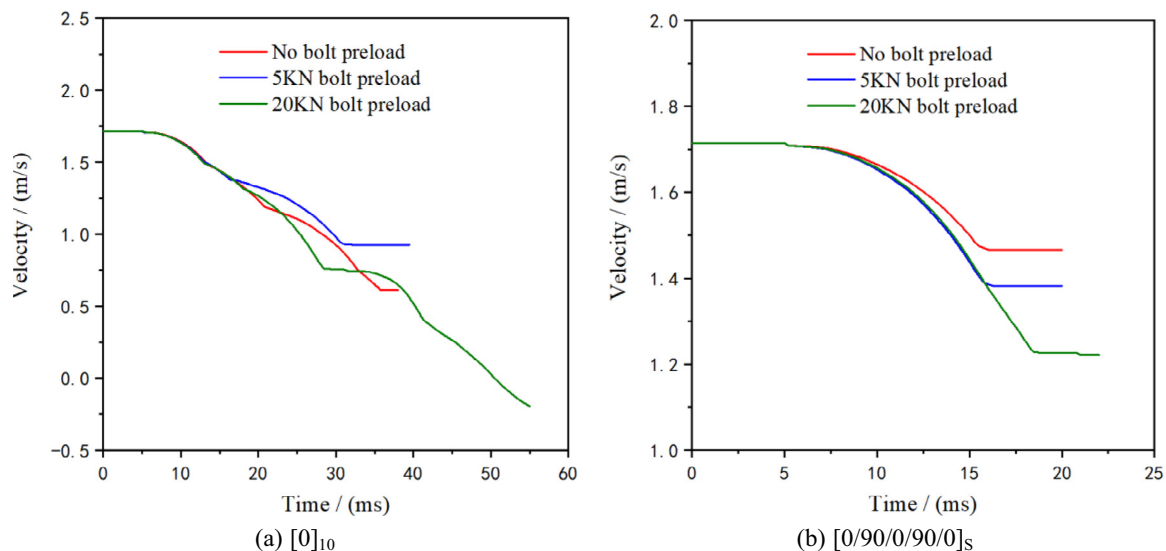

Fig. 9. Speed-time curves of impactor on the two types of protection suspender model considering 0, 5 and 20 kN bolt preload, (a)-[0]$_{10}$ and (b)-[0/90/0/90/0]s.
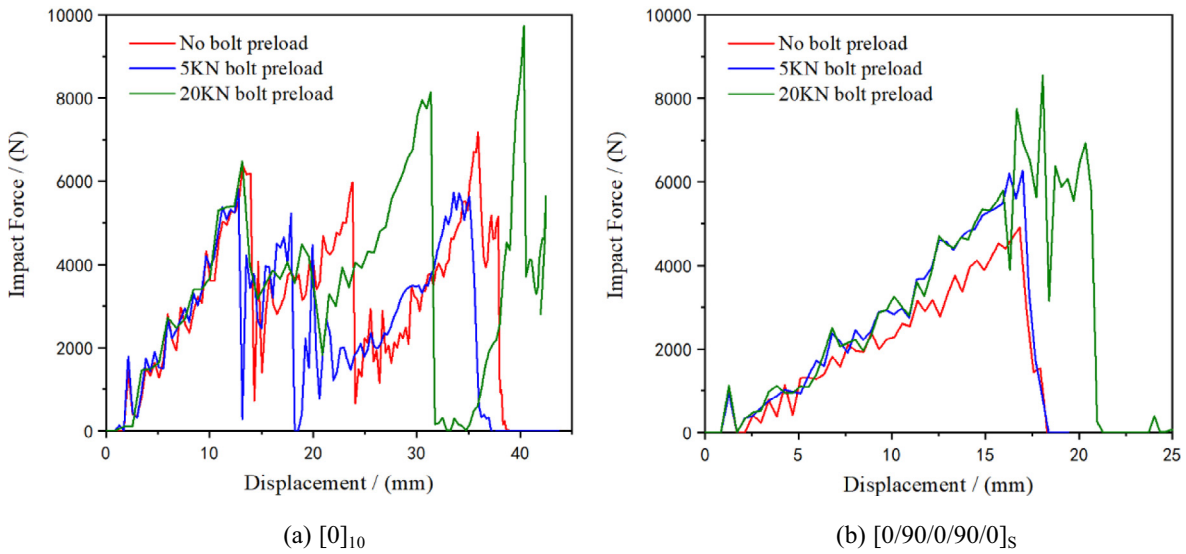
Fig. 10. Impact force–displacement curves of impactor on the protection suspender model with two lay-ups under different bolt preloads: (a)-[0]₁₀ and (b)-[0/90/0/90/0]ₛ.
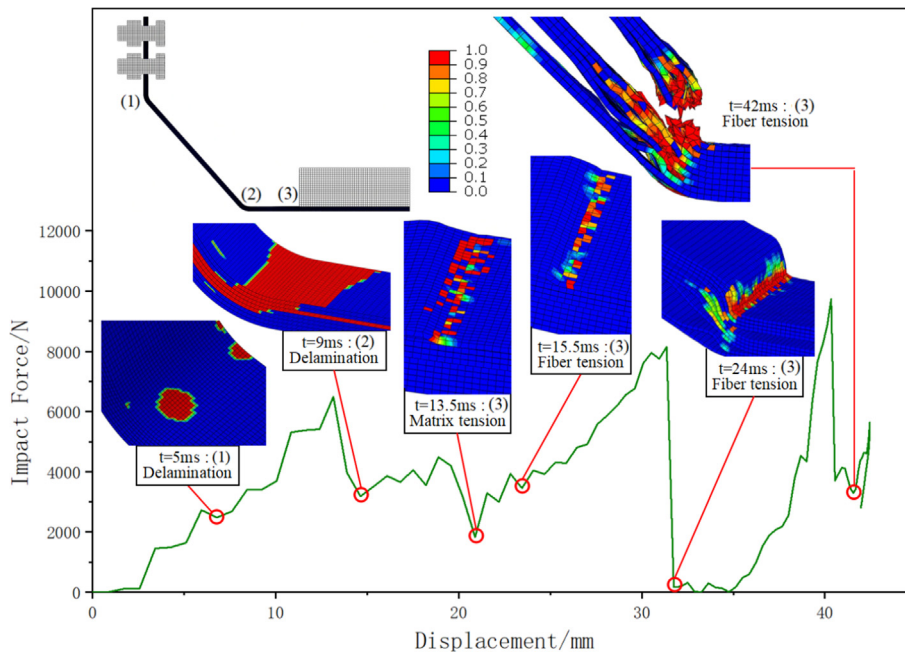

Fig. 11. Impact force–displacement curve of impactor on the [0]₁₀ protection suspender model under 20 kN bolt preload and the damage of protection suspender at different points of time.

cally. At t = 42 ms, the impact event was almost till the end and the damage of protection suspender had evolved to the final stage. At this moment, the fiber tensile damage of some intra-laminar elements at the position (3) reached the limit, therefore the corresponding elements were degraded and several layers of protection suspender were destroyed. When Sun et al. [41] and Aryal et al. [42] studied the low-velocity impact response of sandwich panel, the impact force–displacement curves also show more than one peak of impact force. They believe that the front facesheets are perforated by the impactor and the force reaches a plateau after dropping from the first peak. When the foam material underneath the impactor attains a densified state, the back facesheet starts to bear more load and the force rises again to a second peak. In the present work of this paper, as can be seen from Fig. 11, delamination made the protection suspender divided into multiple

independent single layers or sub-laminates (include several layers) at the position (2) and (3). During the impact, the macro damage will occur first on the top layer or sub-laminate and the first peak and drop will correspond to the destruction of the first ply. As the loading continues, the lower layers will continue to bear the load, the impact force will rise again to another peak until more macro damage and element deletion.

Fig. 12 is the damage contour of the [0/90/0/90/0]ₛ protection suspender. It can be seen from Fig. 12(a), that at t = 18.5 ms, damage in the 90°layers under both the fiber and matrix tension are more severe than that in the 0°layers in all the three positions. This is because, during impact, the stress along the length of protection suspender (the direction P-1 in Fig. 6) is much higher than the stress in other directions. For the 0°layers, its fiber direction is along P-1 direction, but for the 90°layers, the strength along the

P-1 direction is determined by the matrix which is much lower than fiber. Therefore, the 90°layers will be destroyed first and only when the loads exceed a certain criteria, the 0°layers will start to have damage. Fig. 12(b) shows the tensile damage of fiber and matrix at t = 22 ms. As can be seen, from t = 18.5 ms to t = 22 ms, fiber and matrix tensile damage for both the 90°and 0°-layers at the three positions (1), (2) and (3) had been developed and the damage in 90°layers has been developed much faster than that in the 0°layers. In the position (2), the stress gradually concentrated in the 0°layers due to the rapid degradation of material properties for the 90°layers. At t = 22 ms, both the 90°and 0°layers completely reached the limit of capacity, and the protection suspender got destroyed at position (2). During the impact, the damage occurred only at the positions (1), (2) and (3) of protection suspender, and the protection suspender is finally destroyed completely at the position (2). So the positions (1), (2) and (3) are the position under high risk, while the position (2) corresponding to

the edge of the curvature is the weakest part among the three. During design of CFRP protection suspender, the weak positions should be paid special attention.

Fig. 13 is the damage contour of the $[0]_{10}$ FRP protection suspender at the end of the impact with applying 0 and 5 kN bolt preload. The damage of the protection suspender was mainly concentrated in the location (1), (2) and (3), and the damage severity at the position (2) and (3) was obviously greater than that at the position (1). Meanwhile, the fiber and matrix tension damage at position (1) was marginal and only existed on the top layer of the protection suspender. The protection suspender had severe fiber and matrix tension damage in the position (2) and (3) and with obvious delamination there. The location of the maximum damage and failure was dependent on the bolt preload. For the case with bolt preload of 0 kN, the fiber tension damage of all the intra-laminar elements of every layer in the position (3) reached the limit value, so the stiffness of these elements were
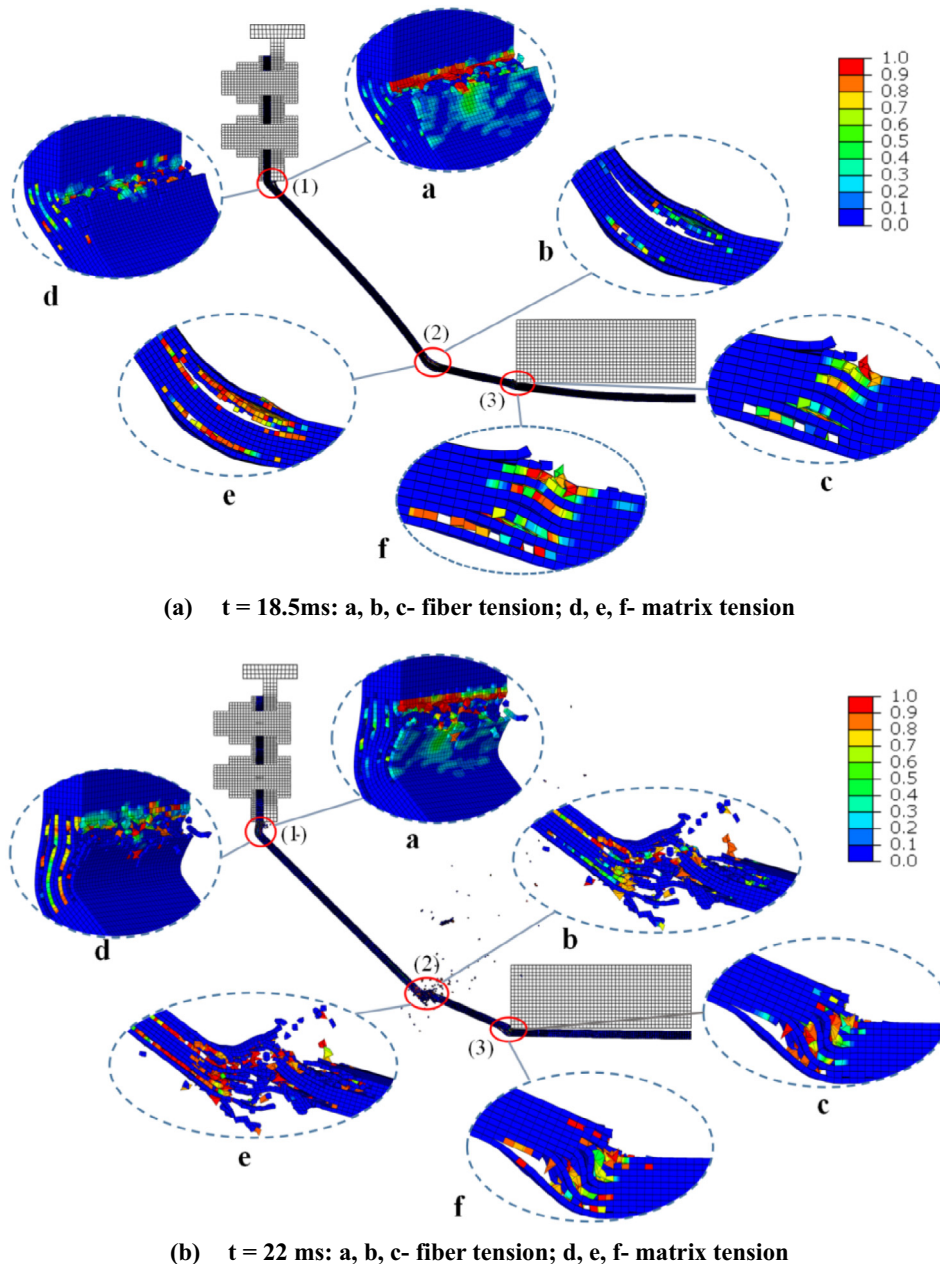

(a)   **t = 18.5ms: a, b, c- fiber tension; d, e, f- matrix tension**

(b)   **t = 22 ms: a, b, c- fiber tension; d, e, f- matrix tension**

Fig. 12. Impact damage in the protection suspender with the lay-up of $[0/90/0/90/0]_S$.

degraded. This means that the protection suspender reached the capacity bearing limit and finally broke completely at the position (3). When the bolt preload was 5 kN, the position (2) was where the protection suspender reached the capacity bearing limit and destroyed completely in the end.

A similar comparison of the damage of the [0/90/0/90/0]$_S$ FRP protection suspender at the end of impact event for the two bolt preload cases is shown in Fig. 14. From the picture we can see that (1), (2) and (3) are still the positions where the protection suspender is prone to damage, and the degree of fiber tension and matrix tension damage at position (2) is significantly greater than that at positions (1) and (3). In contrast to the [0]$_{10}$ FRP protection suspender, the [0/90/0/90/0]$_S$ FRP protection suspender had apparent lower delamination damage at position (2) and (3), and complete failure of large-scale intra-laminar elements appears as the main state of destruction. Generally, the damage of the 90°layers was more serious than that of the 0°layers. It can be seen that

for locations where the material had not failed completely, most of the 90°layers had serious matrix tension damage, but the 0°layers had almost no damage of matrix tension. In addition, according to Fig. 12(b) and Fig. 14, for the [0/90/0/90/0]$_S$ FRP protection suspender, when the bolt preload was 0, 5 and 20 kN, the position where the protection suspender completely broken was in position (2), so it is the most dangerous place after impacted. Among all the impact events of protection suspender shown in Figs. 11-14, the damage of protection suspender shown in Fig. 14(a) and (b) seems to be the most serious (all ply materials at location (2) failed completely) and complex. However, during the impact process, the average values of the ratio of hourglass energy to total energy were both less than 1% for the [0/90/0/90/0]$_S$ protection suspender when the bolt preload were 0 kN and 5 kN, which shows the hourglass mode is well controlled.

For the location of the bolt hole, due to the protection from the washer and the mounting base, the damage occurred here is
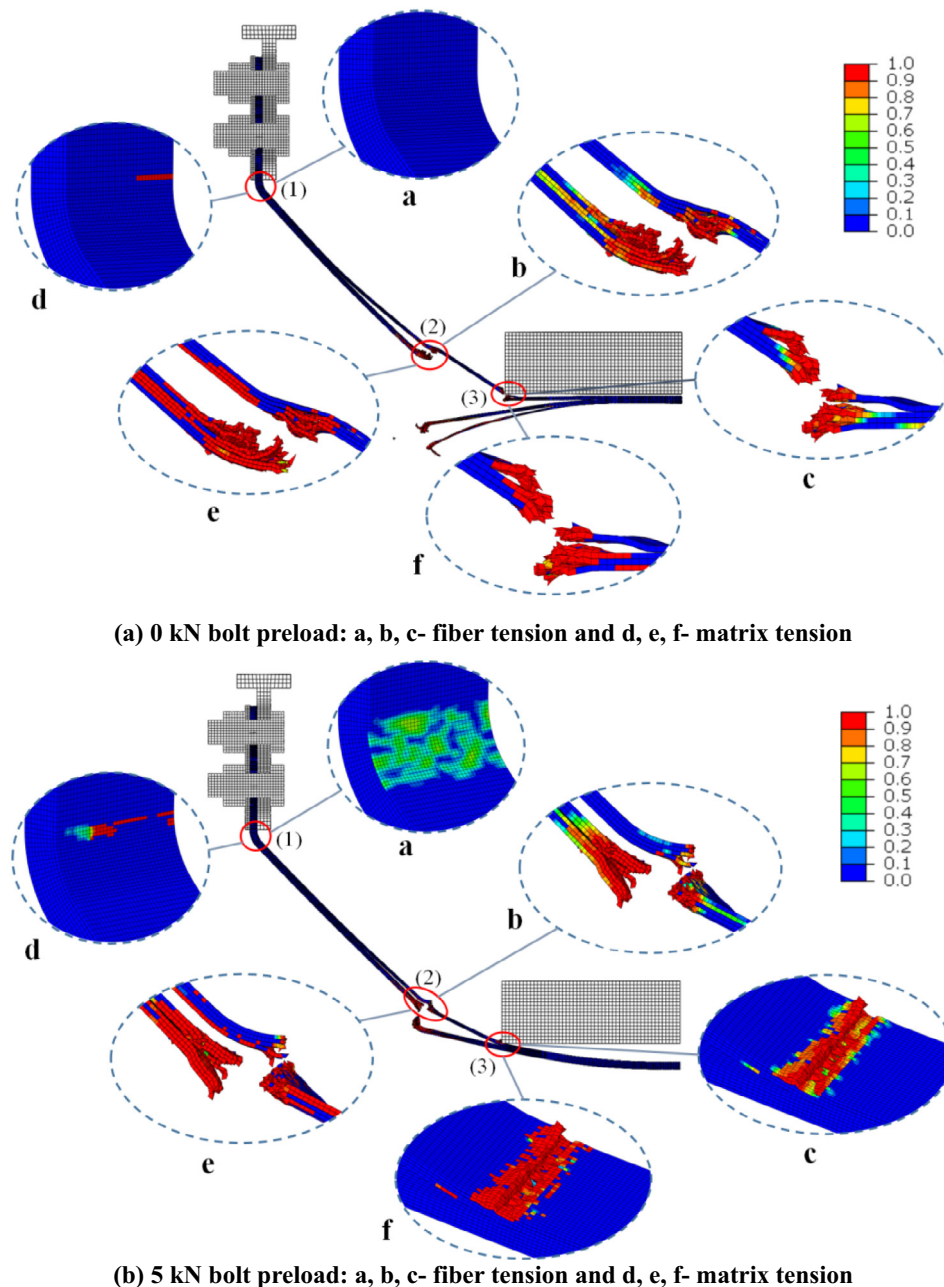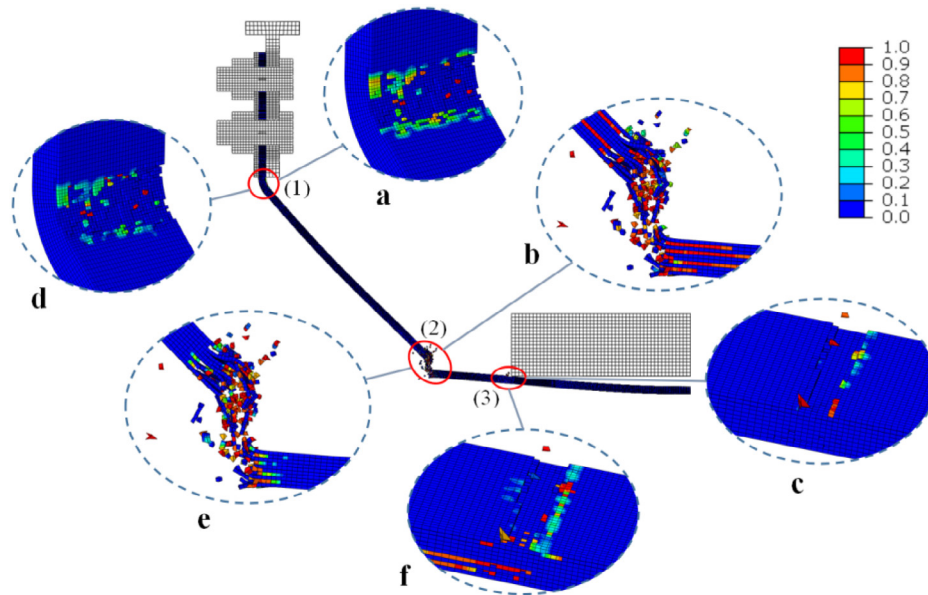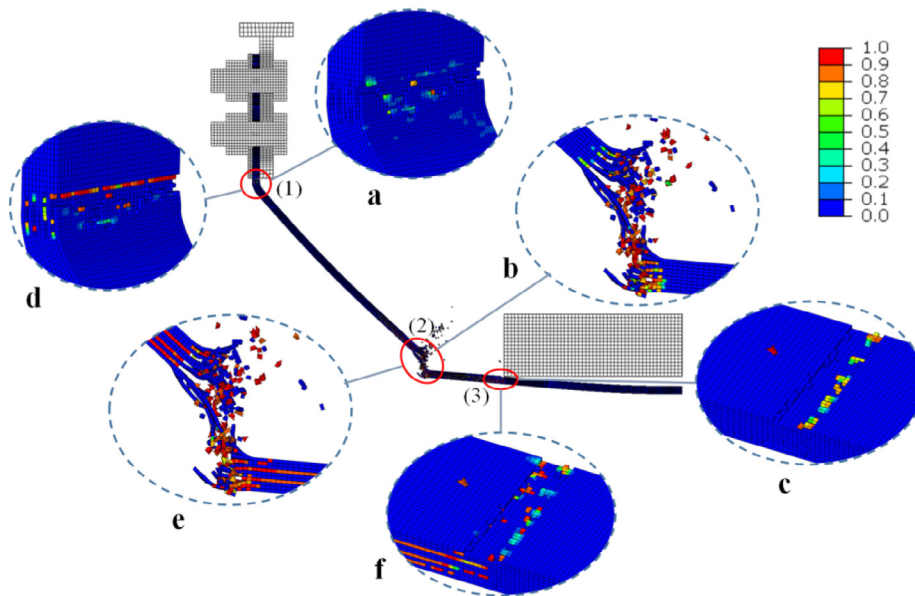

(a) 0 kN bolt preload: a, b, c- fiber tension and d, e, f- matrix tension

(b) 5 kN bolt preload: a, b, c- fiber tension and d, e, f- matrix tension

Fig. 13. Impact damage in the protection suspender with the lay-up of [0]$_{10}$ at the end of the impact event when the bolt preload was: (a) 0 kN and (b) 5 kN.

(a) 0 kN bolt preload: a, b, c- fiber tension and d, e, f- matrix tension

(b) 5 kN bolt preload: a, b, c- fiber tension and d, e, f- matrix tension

Fig. 14. Impact damage in the protection suspender with the lay-up of [0/90/0/90/0]$_S$ at the end of the impact event when the bolt preload was: (a) 0 kN and (b) 5 kN.

relatively low. But the bolt preload has great influence on the position. When the preload is small, there will be damage at the bolt hole. Fig. 15 shows the damage state of [0/90/0/90/0]$_S$ CFRP protection suspender with 0, 5 and 20 kN bolt preload at the end of the impact event. It can be seen from the figure that under the three bolt preloads, there was no delamination damage at the positions of bolt hole. When the bolt preload was 5 and 20 kN, the intra-laminar damage did not occur at the bolt hole also. However, when the bolt preload was 0 kN, the protection suspender had the four types of intra-laminar damage, including fiber tension, fiber compression, matrix tension and matrix compression, at the top of the installation holes. This shows that under the same impact energy, increasing the bolt preload is beneficial to reduce the intra-laminar damage at the bolt hole,

thereby improving the safety performance of the protection suspender when it is impacted. It is worthy to note that under three bolt preloads, the [0]$_{10}$ protection suspender did not show any damage at the bolt holes. This may be because the impact energy has been mostly dissipated by the main body of the strong [0]$_{10}$ protection suspender, and the force transferred from the impact location in the middle of the suspender to the holes in the ends is not as large as that of the [0/90/0/90/0]$_S$ protection suspender. The results are quite interesting since the layers with 90°was expected to help prevent the crack initiation and propagation around the installation holes. Current simulation reveals that the bolt holes of the [0]$_{10}$ protection suspender is much safer during the impact than that of the [0/90/0/90/0]$_S$ protection suspender.
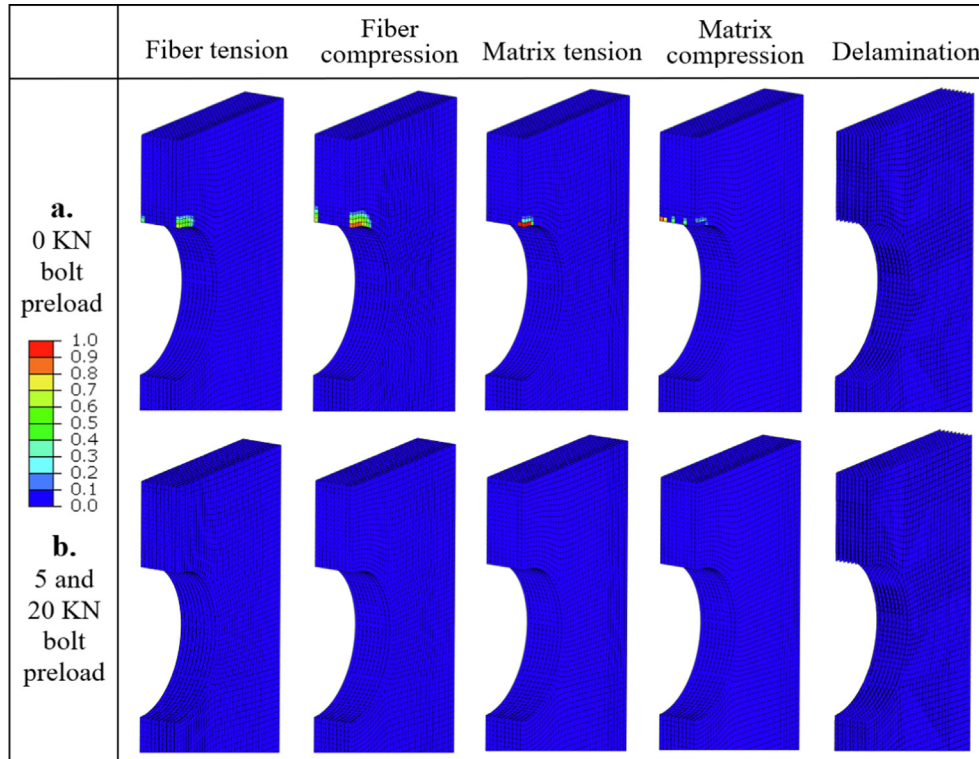
Fig. 15. Damage at the bolt hole of the $[0/90/0/90/0]_S$ protection suspender with different bolt preloads at the end of the impact event: a-0 kN bolt preload and b-5, 20 kN bolt preload.

5. Conclusions

In this paper, a three-dimensional FE model was constructed for studying the low-velocity impact behavior of the CFRP bolster protection suspender. A user-defined VUMAT subroutine written with the constitutive damage model was implemented in ABAQUS/ Explicit solver to calculate the intra-laminar damage and cohesive zone elements were used to evaluate the inter-laminar damage. The vulnerable positions after impact were analyzed for the protection suspender, and the influence of bolt preloads on the protection suspender were also studied for two types of lay-ups.

The following conclusions can be drawn:

1. The energy absorption capability of $[0]_{10}$ protection suspender is always better than $[0/90/0/90/0]_S$ protection suspender. Moreover, the overall load bearing capacity of the 0°layers is much higher than that of the 90°layers during the impact. Therefore, the 0°layers should be set as many as allowed when the CFRP protection suspender is designed to resist low-velocity impact.

2. The locations in the protection suspender which are most vulnerable to impact damage have been identified. Those parts should be paid extra attention during the design stage. The finite element model of the impact response for different layups can be used to optimize the arrangement of FRP materials at these vulnerable positions.

3. Increasing the bolt preloads within an appropriate range can improve the energy absorption capacity of the protection suspender and slow down the development of damage. This can improve the safety of the protection suspender under low-velocity impact. Therefore, when the CFRP protection suspender is installed, simulation can be used to obtain the minimum bolt preload value that provides satisfactory impact damage resistance for the protection suspender.

The present simulation results can help to identify the vulnerable positions of a composite component subjected to impact and have great value for the lightweight design and structural optimization of the composite protection suspender of railway vehicles. Further collaboration with the industry is ongoing and the real application of this simulation-driven design of lightweight components is on the way.

Data availability

The raw data or modeling codes required to reproduce these findings cannot be shared at this time as the data also forms part of an ongoing industry project.

Declaration of Competing Interest

The authors declare that they have no known competing financial interests or personal relationships that could have appeared to influence the work reported in this paper.

References

[1] J.-S. Kim, S.-J. Lee, K.-B. Shin, Manufacturing and structural safety evaluation of a composite train carbody, Compos. Struct. 78 (4) (2007) 468–476.
[2] A. Zinno, E. Fusco, A. Prota, G. Manfredi, Multiscale approach for the design of composite sandwich structures for train application, Compos. Struct. 92 (9) (2010) 2208–2219.

[3] A. Önder, M. Robinson, Harmonised method for impact resistance requirements of E-glass fibre/unsaturated polyester resin composite railway car bodies, Thin-Walled Structures 131 (2018) 151–164.

[4] B. Falzon, W. Tan, Predicting impact damage, residual strength and crashworthiness of composite structures, SAE International Journal of Materials and Manufacturing 9 (3) (2016) 718–728.

[5] A. Sakly, A. Laksimi, H. Kebir, S. Benmedakhen, Experimental and modelling study of low velocity impacts on composite sandwich structures for railway applications, Eng. Fail. Anal. 68 (2016) 22–31.

[6] R. Bogenfeld, J. Kreikemeier, T. Wille, Review and benchmark study on the analysis of low-velocity impact on composite laminates, Eng. Fail. Anal. 86 (2018) 72–99.

[7] J.F. Chen, E.V. Morozov, K. Shankar, A combined elastoplastic damage model for progressive failure analysis of composite materials and structures, Compos. Struct. 94 (12) (2012) 3478–3489.

[8] J.-F. Chen, E.V. Morozov, K. Shankar, Simulating progressive failure of composite laminates including in-ply and delamination damage effects, Compos. A Appl. Sci. Manuf. 61 (2014) 185–200.

[9] Y. Shi, T. Swait, C. Soutis, Modelling damage evolution in composite laminates subjected to low velocity impact, Compos. Struct. 94 (9) (2012) 2902–2913.

[10] Y. Shi, C. Pinna, C. Soutis, Modelling impact damage in composite laminates: a simulation of intra-and inter-laminar cracking, Compos. Struct. 114 (2014) 10–19.

[11] P.F. Liu, J.Y. Zheng, Recent developments on damage modeling and finite element analysis for composite laminates: A review, Mater. Des. 31 (8) (2010) 3825–3834.

[12] J. Zhou, P. Wen, S. Wang, Finite element analysis of a modified progressive damage model for composite laminates under low-velocity impact, Compos. Struct. 225 (2019) 111113, https://doi.org/10.1016/j.compstruct.2019.111113.

[13] Z. Hashin, A. Rotem, A fatigue failure criterion for fiber reinforced materials, J. Compos. Mater. 7 (4) (1973) 448–464.

[14] Z. Hashin, Failure criteria for unidirectional fiber composites, Journa l of Applied Mechanics 47 (2) (1980) 329–334.

[15] F.-K. Chang, K.-Y. Chang, A progressive damage model for laminated composites containing stress concentrations, J. Compos. Mater. 21 (9) (1987) 834–855.

[16] J.P. Hou, N. Petrinic, C. Ruiz, S.R. Hallett, Prediction of impact damage in composite plates, Compos. Sci. Technol. 60 (2) (2000) 273–281.

[17] J.P. Hou, N. Petrinic, C. Ruiz, A delamination criterion for laminated composites under low-velocity impact, Compos. Sci. Technol. 61 (14) (2001) 2069–2074.

[18] Y. Mi, M.A. Crisfield, G.A.O. Davies, H.B. Hellweg, Progressive delamination using interface elements, J. Compos. Mater. 32 (14) (1998) 1246–1272.

[19] P.P. Camanho, C.G. Davila, M.F. de Moura, Numerical simulation of mixed-mode progressive delamination in composite materials, J. Compos. Mater. 37 (16) (2003) 1415–1438.

[20] R. Krueger, Virtual crack closure technique: history, approach, and applications, Appl. Mech. Rev. 57 (2) (2004) 109–143.

[21] G. Gao, S. Wang, Crashworthiness of passenger rail vehicles: a review, Int. J. Crashworthiness 24 (6) (2019) 664–676.

[22] Lian Q L, Liu Z M, Wang W J. Fatigue failure mechanism and improvement method of safety suspender mounting base of speed-up passenger car bogie. Journal of Traffic and Transporation Engineering, 2018, 18(1):71-78. (China)

[23] Y.P. Feng, Research suggestion on the fracture phenomenon of 209P train passenger bogie, Lanzhou Jiaotong University in China), 2015. Master thesis of.

[24] Q. Yang, B. Cox, Cohesive models for damage evolution in laminated composites, Int. J. Fract. 133 (2) (2005) 107–137.

[25] K. Wu, Z. Zheng, S. Zhang, L. He, H. Yao, X. Gong, Y. Ni, Interfacial strength-controlled energy dissipation mechanism and optimization in impact-resistant nacreous structure, Mater. Des. 163 (2019) 107532, https://doi.org/10.1016/j.matdes.2018.12.004.

[26] Z. Pan, F. Qiao, M. Wang, Z. Wu, Z. Ying, A novel damage mechanism analysis of integrally braided CFRP and CFRP/Aluminum hybrid composite tube subjected to transverse impact, Mater. Des. 206 (2021) 109815, https://doi.org/10.1016/j.matdes.2021.109815.

[27] W. Liu, Z. He, F. Yu, G. Qing, A progressive damage model introducing temperature field for bolted composite joint with preload, Modell. Simul. Mater. Sci. Eng. 27 (6) (2019) 065011, https://doi.org/10.1088/1361-651X/ab230f.

[28] N. Tanlak, F.O. Sonmez, E. Talay, Detailed and simplified models of bolted joints under impact loading, The Journal of Strain Analysis for Engineering Design 46 (3) (2011) 213–225.

[29] B. Egan, C.T. McCarthy, M.A. McCarthy, P.J. Gray, R.M. Frizzell, Modelling a single-bolt countersunk composite joint using implicit and explicit finite element analysis, Comput. Mater. Sci. 64 (2012) 203–208.

[30] Z.Y. Qin, S.Z. Yan, F.L. Chu, Finite element analysis of the clamp band joint, Appl. Math. Model. 36 (1) (2012) 463–477.

[31] A. Shipsha, M. Burman, Failure mechanisms in NCF composite bolted joints: Experiments and FE model, Compos. B Eng. 192 (2020) 107950.

[32] C.-H. Huang, Y.-J. Lee, Experiments and simulation of the static contact crush of composite laminated plates, Compos. Struct. 61 (3) (2003) 265–270.

[33] G.-C. Yu, L.-Z. Wu, Li. Ma, J. Xiong, Low velocity impact of carbon fiber aluminum laminates, Compos. Struct. 119 (2015) 757–766.

[34] X. Cheng, J. Zhang, J. Bao, B. Zeng, Y. Cheng, R. Hu, Low-velocity impact performance and effect factor analysis of scarf-repaired composite laminates, Int. J. Impact Eng. 111 (2018) 85–93.

[35] W. He, J. Liu, S. Wang, D.e. Xie, Low-velocity impact response and post-impact flexural behaviour of composite sandwich structures with corrugated cores, Compos. Struct. 189 (2018) 37–53.

[36] I. Lapczyk, J.A. Hurtado, Progressive damage modeling in fiber-reinforced materials, Compos. A Appl. Sci. Manuf. 38 (11) (2007) 2333–2341.

[37] Linde P, Pleitner J, Boer H D, et al. Modelling and simulation of fibre metal laminates// ABAQUS Users' Conference. Boston, Massachustts:[s. n.], 2004: 421-439.

[38] M.L. Benzeggagh, M. Kenane, Measurement of mixed-mode delamination fracture toughness of unidirectional glass/epoxy composites with mixed-mode bending apparatus, Compos. Sci. Technol. 56 (4) (1996) 439–449.

[39] H.J. Wu, Numerical simulation of crack and process improvement of CCKZ63 spring joist, Beijing Jiaotong University in China), 2008. Master thesis of.

[40] Huang X L, Sun L P, Wang Y Y, et al. Structural topological optimization research for railway wagon bolster. Journal of Dalian Jiaotong University, 2013, 34(2):1-5. (China)

[41] G. Sun, E. Wang, H. Wang, Z. Xiao, Q. Li, Low-velocity impact behaviour of sandwich panels with homogeneous and stepwise graded foam cores, Mater. Des. 160 (2018) 1117–1136.

[42] B. Aryal, E.V. Morozov, H. Wang, K. Shankar, P.J. Hazell, J.P. Escobedo-Diaz, Effects of impact energy, velocity, and impactor mass on the damage induced in composite laminates and sandwich panels, Compos. Struct. 226 (2019) 111284, https://doi.org/10.1016/j.compstruct.2019.111284.